



**HAL**  
open science

# Coupling 3D Geomechanics to Classical Sedimentary Basin Modeling: From Gravitational Compaction to Tectonics

A. Brüch, D. Colombo, J. Frey, J. Berthelon, M.C. Cacas-Stentz, T. Cornu, C. Gout

► **To cite this version:**

A. Brüch, D. Colombo, J. Frey, J. Berthelon, M.C. Cacas-Stentz, et al.. Coupling 3D Geomechanics to Classical Sedimentary Basin Modeling: From Gravitational Compaction to Tectonics. *Geomechanics for Energy and the Environment*, 2021, 28, pp.100259. 10.1016/j.gete.2021.100259 . hal-03288049

**HAL Id: hal-03288049**

**<https://ifp.hal.science/hal-03288049>**

Submitted on 16 Jul 2021

**HAL** is a multi-disciplinary open access archive for the deposit and dissemination of scientific research documents, whether they are published or not. The documents may come from teaching and research institutions in France or abroad, or from public or private research centers.

L'archive ouverte pluridisciplinaire **HAL**, est destinée au dépôt et à la diffusion de documents scientifiques de niveau recherche, publiés ou non, émanant des établissements d'enseignement et de recherche français ou étrangers, des laboratoires publics ou privés.

# Coupling 3D Geomechanics to Classical Sedimentary Basin Modeling: From Gravitational Compaction to Tectonics

A. Brüch<sup>1,\*</sup>, D. Colombo<sup>1</sup>, J. Frey<sup>1</sup>, J. Berthelon<sup>1</sup>, M.C. Cacas-Stentz<sup>1</sup>,  
T. Cornu<sup>2</sup>, C. Gout<sup>2</sup>

<sup>1</sup> IFP Energies nouvelles, 1 et 4 avenue de Bois-Préau, 92852 Rueil-Malmaison, France

<sup>2</sup> TOTAL SE, Avenue Larribau, 64018 Pau, France

\* Corresponding author. E-mail address: andre.reinert-bruch@ifpen.fr

**Abstract.** Classical sedimentary basin simulators account for simplified geomechanical models that describe material compaction by means of phenomenological laws relating porosity to vertical effective stress. In order to overcome this limitation and to deal with a comprehensive poromechanical framework, an iterative coupling scheme between a basin modeling code and a mechanical finite element code is adopted. This work focuses on the porous material constitutive law specifically devised to couple 3D geomechanics to basin modeling. The sediment material is considered as an isotropic fully saturated poro-elastoplastic medium undergoing large irreversible strains. Special attention is given to the development of a hardening law capable of reproducing the same porosity evolution as provided by the standard basin simulator when the sediment material is submitted to gravitational compaction under oedometric conditions. A synthetic case is used to illustrate the ability of the proposed workflow to integrate horizontal deformations in the basin model as such effects cannot be captured by the simplified geomechanics of the standard basin code. The results obtained by the coupled simulation demonstrate that horizontal compression may significantly contribute to overpressure development and brittle failure of the basin seal rocks, highlighting the importance of a coupled approach to simulate complex tectonic history.

**Keywords** Sedimentary Basin, Tectonics, Mechanical Compaction, Coupled Geomechanics, Poro-Elastoplasticity, Finite Element Method.

## 1 Introduction

Based on available data and postulated geological scenarios, sedimentary basin modeling seeks to describe the present day state of a basin by solving a complex multi-physics problem through tens to hundreds of millions of years (Allen and Allen, 2005; Hantschel and Kauerauf, 2009). It has been largely used in the last decades by the petroleum exploration industry to locate and estimate the amount of oil and gas in hydrocarbon reservoirs, providing also important information for drilling and production teams regarding fluid overpressure, cap rock integrity and fault stability.

Basin modeling has been nowadays driven to further applications in the context of energy transition as preliminary assessments through large scale simulations may help to find suitable CO<sub>2</sub> storage or geothermal reservoirs by characterizing, for instance, their rock and fluid properties, natural fractures network and hydrothermal fluid circulation (Benjakul et al., 2020; Grigoli et al., 2017; Moscariello, 2019; Stricker et al., 2020; Zappone et al., 2021; Zivar et al., 2020). Simulating the evolution of a sedimentary basin through geological time requires the integration of several coupled phenomena such as sediment compaction, fluid flow and heat transport in order to predict rock porosity and permeability, temperature and heat flow distribution, as well as the identification of critically stressed zones (Bjorlykke, 2010; Gutierrez and Wangen, 2005; Tuncay and Ortoleva, 2004).

In what concerns the mechanical aspects of sedimentary basins, understanding and modeling the burial history of sediments have been the subject of study for a long time

49 (Bjorlykke 2014; Hamilton, 1959; Hedberg, 1936; Schmidt and McDonald, 1979). A major  
50 contribution has been published by Athy (1930) who established an empirical law to describe  
51 rock porosity as an exponential function of burial depth. Later on, Smith (1971) has proposed  
52 to link porosity to vertical effective stress by means of a phenomenological relation. This  
53 equation has been extended by Schneider et al. (1996) by adding additional parameters to  
54 better describe near surface porosity data.

55 The so called Schneider's law is still applied in classical basin simulators to model  
56 mechanical compaction of sediments (Schneider et al., 2000). This relation is based on the  
57 hypothesis of an oedometric evolution of the basin, where deformation is only driven by  
58 sediments overburden. This approach is considered to be suitable for modeling basins which  
59 were not subjected to important horizontal deformation throughout their history. However, it  
60 is not capable to capture the impact of lateral tectonic loadings that may strongly affect its  
61 poromechanical state, leading to overpressure build-up and eventually resulting in seal rock  
62 fracturing and fault reactivation (Berthelon et al., 2021; Hubbert and Rubey, 1959; Maghous  
63 et al., 2014; Obradors-Prats et al., 2017).

64 In order to overcome this limitation and to account for a three-dimensional poromechanical  
65 framework, an iterative coupling scheme between the conventional basin simulator ArcTem  
66 (Faille et al., 2014) and a mechanical finite element code (Code\_Aster) has been developed.  
67 The simplified geomechanics of the standard basin code is then replaced by a full 3D poro-  
68 elastoplastic formulation, which is able to provide a more realistic geomechanical history of  
69 the basin. Beyond that, the decision to integrate an explicit coupling instead of developing an  
70 implicit formulation on the existing basin code stems to the fact that it provides more  
71 flexibility and efficiency in code management (Kim et al., 2011).

72 In this context, three key features must be thoroughly addressed regarding the numerical  
73 aspects of the coupled procedure: a) the formulation of a comprehensive mechanical  
74 description of the geological material relying on a tensorial formalism (Bernaud et al., 2006);  
75 b) the strategy of the staggered solution between codes and the convergence of the  
76 poromechanical problem (Felippa et al., 2001), and c) the geometrical consistency between  
77 the backward and forward basin history (Crook et al., 2018).

78 This work focuses on the porous material constitutive model used in the mechanical code  
79 together with some fundamental aspects of its numerical implementation. Special attention is  
80 given to the development of a hardening law capable of reproducing the same porosity  
81 evolution as provided by the standard basin simulator when the sediment material is submitted  
82 to gravitational compaction under oedometric conditions. Complementary aspects with  
83 respect to the coupling strategy, the backward/forward consistency as well as other theoretical  
84 components of the basin code are not in the scope of this paper. Additional works related to  
85 the geomechanical modeling of sedimentary basins include: Albertz and Sanz (2012),  
86 Barnichon and Charlier (1996), Bruch et al. (2018), Buitter et al. (2009), Crook et al. (2006),  
87 Guy et al. (2019), Jarosinski et al. (2011), Miranda et al. (2020), Obradors-Prats et al. (2019).

88 The constitutive model and main computational aspects are described in sections 2 and 3,  
89 respectively. Section 4 is dedicated to the verification of the material model and the  
90 calibration procedure based on the solution of an oedometric compression test, where  
91 sandstone and shale lithologies have been chosen to illustrate the constitutive model behavior.  
92 Finally, section 5 presents a 3D synthetic case of a sedimentary basin submitted to  
93 gravitational compaction and tectonic loading. The effectiveness of the coupling solution is  
94 discussed through comparison with results provided by the standard basin code before and  
95 after tectonics.

96

97 **2 Constitutive model**

98 The burial history of a layer of sediments involves significant porosity loss. Therefore,  
 99 physical and geometric nonlinearities have to be considered in the formulation of the  
 100 constitutive model to represent the porous material behavior throughout the compaction  
 101 process. In this work, the sediment material is considered as an isotropic fully saturated poro-  
 102 elastoplastic medium undergoing large irreversible strains. The continuum mechanics sign  
 103 convention is adopted, i.e. compressive stresses are negative.

104 **2.1 State equation and complementary laws**

105 In the framework of finite poroplasticity, the macroscopic rate equation of state involves a  
 106 rotational time derivative  $D_J/Dt$  of the Terzaghi effective stress tensor  $\underline{\underline{\sigma}}' = \underline{\underline{\sigma}} + p\underline{\underline{1}}$   
 107 (Dormieux and Maghous, 1999):

$$\frac{D_J \underline{\underline{\sigma}}'}{Dt} = \underline{\underline{\dot{\sigma}}}' + \underline{\underline{\sigma}}' \cdot \underline{\underline{\Omega}} - \underline{\underline{\Omega}} \cdot \underline{\underline{\sigma}}' = \underline{\underline{C}} : (\underline{\underline{d}} - \underline{\underline{d}}^p) \quad (1)$$

108 where  $\underline{\underline{\sigma}}$  is the Cauchy total stress tensor,  $p$  is the pore-fluid pressure,  $\underline{\underline{d}}$  and  $\underline{\underline{d}}^p$  are  
 109 respectively the total and plastic part of the strain rate tensor and  $\underline{\underline{\Omega}}$  is the spin rate tensor.  
 110 The fourth-order tensor  $\underline{\underline{C}}$  is the material drained elastic stiffness moduli and reads by virtue  
 111 of isotropy assumption:

$$\underline{\underline{C}} = (K - 2\mu/3)\underline{\underline{1}} \otimes \underline{\underline{1}} + 2\mu \underline{\underline{1}} \quad (2)$$

112 where  $\underline{\underline{1}}$  and  $\underline{\underline{1}}$  refer to the second and fourth-order identity tensors whereas  $K$  and  $\mu$  denote  
 113 the bulk and shear moduli, respectively. The latter are expected to increase with burial due to  
 114 microstructural changes resulting from compaction: large macroscopic plastic strains are  
 115 associated with an irreversible evolution of the microstructure, which is responsible for  
 116 variations of the macroscopic elastic properties of the porous medium (Bernaud et al., 2002;  
 117 Nooraiepour et al., 2017). This stiffness increase is addressed in the model by means of the  
 118 Hashin-Shtrikman upper bounds (Hashin, 1983), which are known to reasonably describe the  
 119 elastic properties of isotropic porous media (Zaoui, 2002). The expressions for the bulk and  
 120 shear moduli of the porous material are given as functions of the bulk and shear moduli of the  
 121 solid phase,  $k^s$  and  $\mu^s$ , and the Eulerian porosity  $\varphi$ :

$$K(\varphi) = \frac{4k^s \mu^s (1 - \varphi)}{3k^s \varphi + 4\mu^s} \quad (3)$$

$$\mu(\varphi) = \frac{\mu^s (1 - \varphi) (9k^s + 8\mu^s)}{k^s (9 + 6\varphi) + \mu^s (8 + 12\varphi)} \quad (4)$$

122 The Eulerian porosity defines the pore space volume fraction in the current configuration  
 123 of the porous elementary volume. It is a key parameter of the model as it serves to  
 124 characterize its constitutive and transport properties. It is thus of major importance to define  
 125 an evolution law to quantify porosity change as a function of the irreversible (plastic)  
 126 densification of the porous material.

127 Assuming that the reversible (elastic) strains are infinitesimal, the Jacobian of the skeleton  
 128 transformation defining the ratio between the porous element volume in its current and initial  
 129 configurations can be approximated by the Jacobian of the plastic transformation,  $J \approx J^p$ . In

130 addition, the solid phase is considered to be incompressible during the irreversible  
 131 transformation, which means that any variation of volume during plastic deformation is only  
 132 due to porosity change. These considerations allow to compute the evolution of the porosity  
 133  $\varphi$  as a function of the plastic Jacobian  $J^p$  (Bernaud et al., 2006):

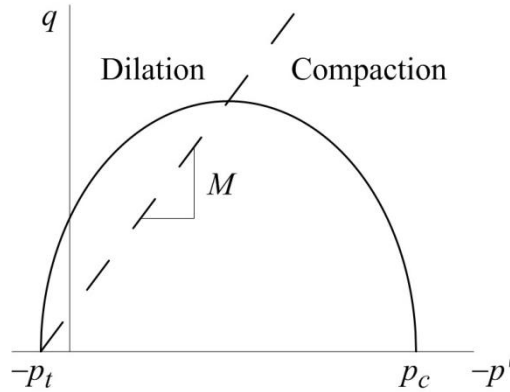
$$\varphi = 1 - \frac{1 - \varphi_0}{J^p} \quad (5)$$

## 134 2.2 Plastic yield surface and flow rule

135 The plastic component of the model represents the mechanical compaction resulting from  
 136 rearrangement of the solid particles during burial. The yield surface represented in Fig. 1 is  
 137 based on the modified Cam-Clay model (Wood, 1990):

$$f(\underline{\underline{\sigma}}', p_c) = q^2 + M^2(p' - p_t)(p' + p_c) \quad (6)$$

138 where  $q = \sqrt{(3/2)\underline{\underline{s}}:\underline{\underline{s}}}$  is the equivalent deviatoric stress,  $\underline{\underline{s}} = \underline{\underline{\sigma}} - \text{tr}\underline{\underline{\sigma}}/3\mathbf{1}$  is the deviatoric  
 139 stress tensor and  $p' = \text{tr}\underline{\underline{\sigma}}'/3$  is the mean effective stress. Parameter  $M$  is related to the  
 140 Mohr–Coulomb friction angle and defines the slope of the line that intersects the yield surface  
 141 at the tensile intercept  $p_t$  of the hydrostatic axis and the  $q$  peak value (Neto et al., 2008). The  
 142 consolidation pressure  $p_c$  defines the compressive intercept of the hydrostatic axis and  
 143 represents the hardening parameter of the model.  
 144



145 **Fig. 1.** Schematic representation of the plastic yield surface.  
 146

147 The flow rule adopted for the plastic strain rate reads:

$$\underline{\underline{d}}^p = \dot{\chi} \frac{\partial g}{\partial \underline{\underline{\sigma}}'} \quad (7)$$

148 where  $\dot{\chi}$  is the non-negative plastic multiplier and  $g$  is the plastic potential:

$$g(\underline{\underline{\sigma}}', p_c) = q^2 + N^2(p' - p_t)(p' + p_c) \quad (8)$$

149 Eq. (8) for the plastic potential differs from eq. (6) defining the yield surface through  
 150 parameter  $N$ . When the stress state is located above the  $M$  line, the value of this parameter  
 151 relates to the dilatancy angle in order to control excessive porosity increase during shear-  
 152 induced dilation, resulting in a non-associated flow rule. For a stress state located below the  
 153  $M$  line (compaction), parameter  $N$  is taken equal to  $M$ , resulting in an associated flow rule.

154 Such conditions can be defined as:

$$N < M \text{ for } p' > -\frac{p_c - p_t}{2} \quad (9)$$

$$N = M \text{ for } p' \leq -\frac{p_c - p_t}{2} \quad (10)$$

155 It must be noted that assuming purely mechanical aspects as the only mechanisms of  
156 porosity reduction may be considered as an oversimplified approach. In reality, the diagenetic  
157 processes transforming sediments into rock are much more complex and different  
158 mechanisms such as pressure solution may predominate at deeper layers of the basin, where  
159 stresses and temperature are elevated (Schmidt and McDonald, 1979; Tada and Siever, 1989).

### 160 2.3 Hardening law in the context of basin modeling

161 The hardening law that describes the evolution of the consolidation pressure as a function  
162 of large plastic strains is a crucial feature of the model as parameter  $p_c$  controls the size of  
163 the yield surface. It is of major importance in the context of sedimentary basin modeling as it  
164 controls how porosity changes during burial.

165 Let us first recall that in the context of small strain plasticity, the classical hardening law in  
166 the Cam-Clay model can be written as a function of the plastic volumetric strain  $\epsilon^p$  and a  
167 material constant  $\alpha$  that can be fitted from isotropic compression tests (Borja and Lee, 1990):

$$p_c = p_{c0} \exp(-\alpha \epsilon^p) \quad (11)$$

168 An important assumption of the Cam-Clay model is that eq. (11) remains valid under non  
169 isotropic loadings. This implies that the effect of the deviatoric plastic strain on the hardening  
170 phenomenon is considered negligible. In other words, it is assumed that hardening is  
171 controlled by plastic densification (Guéguen et al., 2004).

172 A simple way to generalize eq. (11) in the domain of large strains consists in replacing  $\epsilon^p$   
173 by  $J^p - 1$ , since both quantities are equal in the range of small plastic strains (Bernaud et al.,  
174 2002):

$$p_c = p_{c0} \exp(-\alpha(J^p - 1)) \quad (12)$$

175 However, such a hardening law does not enforce the condition  $J^p > 1 - \varphi_0$ , corresponding  
176 to total pore closure, which may lead the sediment material to negative porosities under high  
177 isotropic compression (Deudé et al., 2004). To overcome this issue, a micromechanics-based  
178 law has been proposed by Barthélémy et al. (2003) with the advantage that  $p_c$  tends towards  
179 infinity when the pore space vanishes:

$$p_c = p_{c0} \frac{\ln \varphi}{\ln \varphi_0} \quad (13)$$

180 This formulation has been recently modified by Bruch et al. (2019) using a calibration  
181 exponent  $m$  to predict more realistic porosity distribution curves for different lithologies,  
182 proving to be relevant to represent the compaction trend of clays:

$$p_c = p_{c0} \left( \frac{\ln \varphi}{\ln \varphi_0} \right)^m \quad (14)$$

183 Even though eq. (14) may reasonably model the mechanical compaction of sediments, it  
 184 does not permit to properly reproduce the variation of porosity with burial under oedometric  
 185 conditions as done by the basin code, which is one of the assumptions of this work. Therefore  
 186 a new hardening law must be formulated.

## 187 **2.4 Formulation of a new hardening law**

188 Before working on the mathematical formulation of the new hardening law, a brief review  
 189 of the evolution of sedimentary basins compaction laws is presented.

190 One of the first empirical laws was formulated by Athy (1930), describing rock porosity as  
 191 a function of the burial depth  $z$  and a decay factor  $\beta$ :

$$\varphi = \varphi_0 \exp(\beta z) \quad (15)$$

192 Based on similar assumptions and relying on Terzaghi's concepts, Smith (1971) proposed  
 193 a phenomenological relationship to estimate porosity as a function of the vertical effective  
 194 stress  $\sigma'_v$  and a lithology dependent parameter  $E$  as follows:

$$\varphi = \varphi_0 \exp(\sigma'_v / E) \quad (16)$$

195 The basin code used in this work relies on the porosity law developed by Schneider et al.  
 196 (1996), who extended eq. (16) by introducing a residual porosity  $\varphi_r$  and a second exponential  
 197 term to better fit field data:

$$\varphi = \varphi_r + \varphi_a \exp(\sigma'_v / E_a) + \varphi_b \exp(\sigma'_v / E_b) \quad (17)$$

198 where  $\varphi_a$ ,  $\varphi_b$ ,  $E_a$  and  $E_b$  are calibration coefficients. It must be noted that at surface  $\sigma'_v = 0$   
 199 , thus the initial condition corresponds to  $\varphi_0 = \varphi_r + \varphi_a + \varphi_b$ .

200 The development of the expression for  $p_c$  permitting to obtain from the mechanical code  
 201 the same porosity as the one given by the basin code during gravitational compaction requires  
 202 first the extension to the three-dimensional case of the one-dimensional compaction law (17).  
 203 One possible way to proceed is to rewrite Schneider's law as a function of the mean effective  
 204 stress:

$$\varphi = \varphi_r + \varphi_a \exp(p' / C_a) + \varphi_b \exp(p' / C_b) \quad (18)$$

205 where  $C_a$  and  $C_b$  are calibration coefficients related to  $p'$ .

206 The next step consists of identifying the hardening law from the response of a  
 207 representative elementary volume (REV) undergoing plastic deformation due to an isotropic  
 208 compression together with the phenomenological law of eq. (18). According to the plastic  
 209 yield surface, the loading representing the isotropic compression is a uniform pressure  
 210  $p' = -p_c$  applied to the boundary of the REV. The corresponding effective stress is  $\underline{\underline{\sigma}}' = -p_c \underline{\underline{1}}$   
 211 . By substituting the current effective stress, eq. (18) can be rewritten as:

$$\varphi = \varphi_r + \varphi_a \exp(-p_c / C_a) + \varphi_b \exp(-p_c / C_b) \quad (19)$$

212 In the case  $\varphi_b = 0$ , an analytical expression for  $p_c$  can be straightforwardly derived:

$$p_c = C_a \ln \left( \frac{\varphi_a}{\varphi - \varphi_r} \right) \quad (20)$$

213 Assuming that at its initial state  $\varphi = \varphi_0$  the sediment material has no compressive strength,

214  $p_c = 0$ , eq. (20) gives  $\varphi_a = \varphi_0 - \varphi_r$ . The hardening law can now be rewritten as:

$$215 \quad p_c = C \ln \left( \frac{\varphi_0 - \varphi_r}{\varphi - \varphi_r} \right) \quad (21)$$

216 The calibration coefficient  $C$  controls the evolution of the hardening parameter  $p_c$  with  
 217 respect to porosity change. Depending on the nature of the sediment material, the  
 218 microstructural changes resulting from mechanical compaction may lead to different material  
 219 strength, and for the same compaction level, higher values of  $C$  will result in higher values of  
 220  $p_c$ . By analogy with parameter  $E$  of Smith's law (16), higher values of  $C$  would result in  
 221 higher porosity values for a given basin depth.

222 This expression is limited to representing the porosity trend of a single exponential  
 223 compaction law as it has been derived in the case of  $\varphi_b = 0$ . To circumvent this limitation and  
 224 based on the same reasoning of eq. (14), an exponent  $m$  is applied in an attempt to properly  
 represent the general Schneider's law (17) used by the sedimentary basin code:

$$225 \quad p_c = C \ln \left( \frac{\varphi_0 - \varphi_r}{\varphi - \varphi_r} \right)^m \quad (22)$$

226 The resulting hardening law (22) is used in the present work to represent the porous  
 227 material behavior in the mechanical code. It can be verified that  $p_c \rightarrow +\infty$  when  $\varphi \rightarrow \varphi_r$ ,  
 228 excluding the possibility to have porosities lower than the residual value. The verification of  
 the model is presented in section 4.

### 229 **3 Computational aspects**

230 The mechanical problem is solved by means of the finite element method. The solution of  
 231 the problem is achieved by solving at each instant of time a specific boundary value problem  
 232 formulated on the geometrical domain  $\Omega$  of the considered material system. It is defined by  
 233 the field, constitutive and complementary equations, and completed by the initial values of all  
 234 field variables together with the boundary conditions that should be prescribed on the  
 235 boundary  $\partial\Omega$  of  $\Omega$ .

#### 236 **3.1 Formulation of the mechanical problem**

237 Disregarding inertial effects, the momentum balance equation for the porous continuum  
 238 reads:

$$\text{div } \underline{\underline{\sigma}} + \rho \underline{\underline{g}} = 0 \quad (23)$$

239 where  $\underline{\underline{g}}$  is the acceleration of gravity and  $\rho = (1 - \varphi)\rho^s + \varphi\rho^f$  is the density of the fluid  
 240 saturated porous medium, with  $\rho^s$  and  $\rho^f$  corresponding to the mass densities of the solid  
 241 and fluid phases (Coussy, 2004).

242 The discretized form of the mechanical problem is obtained from weak formulation of the  
 243 equilibrium equation at time  $t' = t + \Delta t$  (unknown configuration) employing piecewise linear  
 244 functions for the displacement  $\underline{U}$  (Zienkiewicz and Taylor, 2000). The updated Lagrangian  
 245 scheme (Bathe, 1996) is used to calculate the finite element solution between the  
 246 configuration at time  $t$  (updated reference configuration) and that at time  $t'$ . The unknown  
 247 variables are then updated at each time step  $\Delta t$ .

248 Denoting by  ${}^t \underline{x}$  the coordinate vector of a sediment particle at time  $t$ , the boundary value  
 249 problem is formulated in terms of displacement  $\underline{U}$  of the particle between  $t$  and  $t'$ :

$$\underline{U} = {}^t \underline{x} - {}^t \underline{x} \quad (24)$$

250 The pore-pressure field obtained from the basin code is discretized in time according to the  
 251 mechanical scheme. The pressure variation at points similar within the porous material reads:

$$P = p({}^t \underline{x}) - p({}^t \underline{x}) = \Delta t {}^t \dot{p} \quad (25)$$

252 The variation of the stress tensor is defined as:

$${}^t \underline{\underline{\sigma}} - {}^t \underline{\underline{\sigma}} = \Delta t {}^t \underline{\underline{\dot{\sigma}}} \quad (26)$$

253 The Eulerian strain rate tensor  ${}^t \underline{\underline{d}}$  and the rotation rate tensor  ${}^t \underline{\underline{\Omega}}$  are approximated by:

$${}^t \underline{\underline{d}} = \frac{1}{\Delta t} \left\{ {}^t \underline{\underline{\nabla U}} \right\}_s \quad (27)$$

$${}^t \underline{\underline{\Omega}} = \frac{1}{\Delta t} \left\{ {}^t \underline{\underline{\nabla U}} \right\}_a \quad (28)$$

254 The hypothesis of infinitesimal transformation is adopted by respecting the condition  
 255  $\left| {}^t \underline{\underline{\nabla U}} \right| \ll 1$  for each time step. In fact, the norm of the displacement gradient is verified for  
 256 each converged step and, if it does not respect a required criterion, the corresponding time  
 257 step is automatically subdivided and recalculated in order to ensure this condition. As a  
 258 consequence, the geometrical nonlinearities can be disregarded in the numerical procedure.  
 259 Accordingly, the resulting expression of the state equation for time  $t'$  is:

$${}^t \underline{\underline{\sigma}} = {}^t \underline{\underline{\sigma}} + {}^t \underline{\underline{C}}^{ep} : \left\{ {}^t \underline{\underline{\nabla U}} \right\}_s - P \underline{\underline{1}} \quad (29)$$

260 where  $\underline{\underline{C}}^{ep}$  accounts for the consistent tangent stiffness operator.

261 The mechanical problem is then solved for time  $t'$  by substituting eq. (29) in the weak  
 262 form of the equilibrium eq. (23), considering  ${}^t \underline{\underline{C}} \approx {}^t \underline{\underline{C}}$ ,  ${}^t \rho \approx {}^t \rho$ ,  $\partial \Omega_t \approx \partial \Omega_t$  and  $\Omega_t \approx \Omega_t$ .  
 263 These approximations imply that the only nonlinear term in the formulation concerns the  
 264 fourth order tensor  ${}^t \underline{\underline{C}}^{ep}$  due to the plastic evolution of the porous material. It is worth  
 265 mentioning that the local integration of the plastic strains is performed based on a  
 266 generalization of the fully implicit return mapping algorithm proposed by Nguyen (1977).

### 267 3.2 Tangent operator

268 In order to enhance the convergence rate of the iterative solution of the mechanical  
 269 problem, the consistent tangent stiffness operator must be derived (Crisfield, 1991).  
 270 Disregarding the terms involving the spin rate tensor, the state equation reads:

$$\underline{\underline{\dot{\sigma}}} = \underline{\underline{C}} : \left( \underline{\underline{d}} - \underline{\underline{d}}^p \right) \quad (30)$$

271 Taking the first order approximation of the plastic strain rate flow rule:

$$\underline{\underline{d}}^p = \dot{\chi} \frac{\partial g}{\partial \underline{\underline{\sigma'}}} + \Delta\chi \frac{\partial^2 g}{\partial \underline{\underline{\sigma'}}^2} : \underline{\underline{\dot{\sigma}'}} \quad (31)$$

272 Substituting the strain rate (31) in eq. (30) gives:

$$\underline{\underline{\dot{\sigma}'}} = \underset{\sim}{R} : \left( \underline{\underline{d}} - \dot{\chi} \frac{\partial g}{\partial \underline{\underline{\sigma'}}} \right) \quad (32)$$

273 where the fourth-order tensor  $\underset{\sim}{R}$  is defined as:

$$\underset{\sim}{R} = \left( \underset{\sim}{C}^{-1} + \Delta\chi \frac{\partial^2 g}{\partial \underline{\underline{\sigma'}}^2} \right)^{-1} \quad (33)$$

274 The plastic consistency condition  $\dot{f} = 0$  reads:

$$\dot{f} = \frac{\partial f}{\partial \underline{\underline{\sigma'}}} : \underline{\underline{\dot{\sigma}'}} + \frac{\partial f}{\partial p_c} \frac{\partial p_c}{\partial \Delta\chi} \dot{\chi} = 0 \quad (34)$$

275 Eqs. (32) and (34) allow to obtain the plastic multiplier  $\dot{\chi}$ :

$$\dot{\chi} = \frac{\frac{\partial f}{\partial \underline{\underline{\sigma'}}} : \underset{\sim}{R} : \underline{\underline{d}}}{\frac{\partial f}{\partial \underline{\underline{\sigma'}}} : \underset{\sim}{R} : \frac{\partial g}{\partial \underline{\underline{\sigma'}}} - \frac{\partial f}{\partial p_c} \frac{\partial p_c}{\partial \Delta\chi}} \quad (35)$$

276 To symmetrize the fourth order tensor that will be used to construct the mechanical  
277 stiffness matrix, an additional scalar is introduced (Luo et al., 2013):

$$\gamma = \frac{\frac{\partial g}{\partial \underline{\underline{\sigma'}}} : \underset{\sim}{R} : \underline{\underline{d}}}{\frac{\partial f}{\partial \underline{\underline{\sigma'}}} : \underset{\sim}{R} : \underline{\underline{d}}} \quad (36)$$

278 Multiplying and dividing eq. (35) by  $\gamma$ :

$$\dot{\chi} = \frac{\frac{\partial g}{\partial \underline{\underline{\sigma'}}} : \underset{\sim}{R} : \underline{\underline{d}}}{\gamma \left( \frac{\partial f}{\partial \underline{\underline{\sigma'}}} : \underset{\sim}{R} : \frac{\partial g}{\partial \underline{\underline{\sigma'}}} - \frac{\partial f}{\partial p_c} \frac{\partial p_c}{\partial \Delta\chi} \right)} \quad (37)$$

279 Finally, by substituting  $\dot{\chi}$  in (32):

$$\underline{\underline{\dot{\sigma}'}} = \underset{\sim}{C}^{ep} : \underline{\underline{d}} \quad (38)$$

280 where the symmetric tensor of the consistent tangent moduli reads:

$$C^{\text{ep}} = R - \frac{R : \frac{\partial g}{\partial \underline{\underline{\sigma'}}} \otimes \frac{\partial g}{\partial \underline{\underline{\sigma'}}} : R}{\gamma \left( \frac{\partial f}{\partial \underline{\underline{\sigma'}}} : R : \frac{\partial g}{\partial \underline{\underline{\sigma'}}} - \frac{\partial f}{\partial p_c} \frac{\partial p_c}{\partial \Delta \chi} \right)} \quad (39)$$

### 281 3.3 Coupling the mechanical and basin codes

282 Once the mechanical problem is solved as described in section 3.1, its solution has to be  
 283 transmitted to the basin code. The objective is to integrate the porosity change induced by  
 284 horizontal deformations in the sedimentary basin model. This is achieved by means of an  
 285 iterative coupling scheme presented in Fig. 2 and briefly described in the remaining part of  
 286 this section.

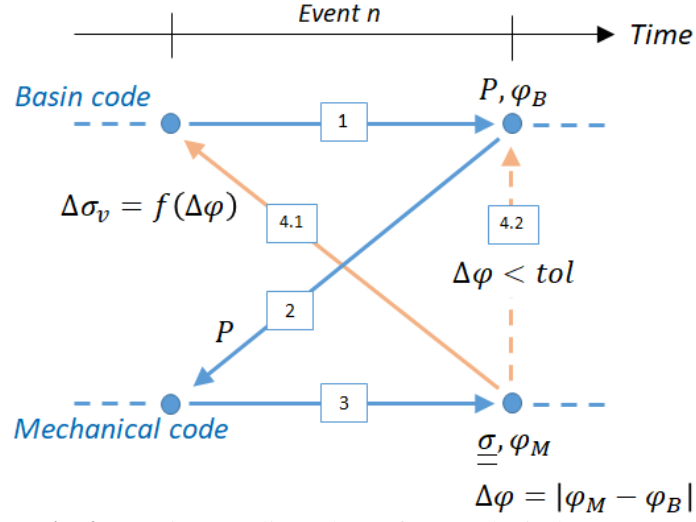
287 The basin history is defined in the standard basin code by a sequence of geological events.  
 288 The coupling strategy considers these events as the time periods for which the staggered  
 289 solution between the basin and mechanical codes should be repeated until convergence is  
 290 reached. During these periods, each code has its own time discretization and independent  
 291 porosity evaluation. Therefore, the convergence criterion used for the iterative coupling is  
 292 based on the porosity difference between the two codes.

293 For a given geological event  $n$ , the first calculation is performed by the basin code. The  
 294 pore-pressure  $P$  obtained at the end of the geological event is transmitted to the mechanical  
 295 code and applied to eq. (29) to solve the equilibrium problem. The porosity distribution  $\varphi_M$   
 296 resulting from the 3D geomechanics solution is then compared to the porosity values  $\varphi_B$   
 297 obtained from the simplified compaction law of the basin simulator. If the porosity difference  
 298  $\Delta\varphi = |\varphi_M - \varphi_B|$  is lower than a user defined tolerance, the numerical simulation proceeds to  
 299 the next event. Otherwise, a corrective term  $\Delta\sigma_v$  is applied to correct the inconsistency  
 300 between the porosity computed from both codes and the event is computed again. This type of  
 301 predictor-corrector approach is well known for coupling geomechanics to reservoir simulation  
 302 (Mainguy and Longuemare, 2002).

303 Keeping in mind that the basin code evaluates porosity change as a function of the vertical  
 304 effective stress  $\sigma'_v = \sigma_v + p$  through eq. (17), the corrective term  $\Delta\sigma_v$  integrates the effects  
 305 of the deformation field obtained in the mechanical code. For the  $i$ th iteration of the staggered  
 306 procedure, the vertical stress considered in the basin code reads:

$$\sigma_{v,i+1} = \sigma_{v,i} + \Delta\sigma_{v,i} \quad (40)$$

307 Depending on the permeability distribution of the basin, the corrective term  $\Delta\sigma_v$  will  
 308 affect the porosity and/or the pore-pressure fields in the basin code. The scheme is repeated  
 309 up to porosity convergence.



310  
311

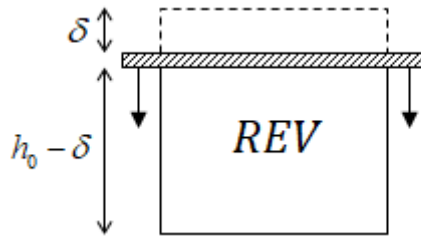
Fig. 2. Iterative coupling scheme for a geological event.

#### 312 4 Verification of the material model

313 This section illustrates the capability of the constitutive model to reproduce the same  
314 porosity evolution of the basin code when submitted to gravitational compaction. The  
315 verification procedure is based on the solution of a representative elementary volume of the  
316 porous material subjected to a prescribed uniaxial strain parallel to the vertical direction  $\underline{e}_v$ ,  
317 i.e. oedometric compression. The REV represents a macroscopic particle of the sediment  
318 material undergoing compaction during burial.

##### 319 4.1 Oedometric compression problem

320 Fig. 3 presents the geometry and loading of the model. The problem is treated in drained  
321 conditions (no excess pore-pressure). In its initial configuration, the REV is a parallelepipedic  
322 domain  $\Omega_0$  of height  $h_0$  and horizontal sides  $l_0$ . The response of the REV to increasing  
323 values of displacement  $\delta$  is supposed to simulate the stress and deformation of particles  
324 located at increasing depths of a sedimentary basin.  
325



326  
327

Fig. 3. Geometry and loading of the model.

328 Starting from  $\delta(t=0)=0$ , the loading process consists in prescribing a continuously  
329 increasing displacement function  $\delta$ . The initial state of stress is natural,  $\underline{\sigma}(t=0)=0$ . The  
330 mechanical response of the REV is determined at any stage of compaction level  $\delta/h_0$ . Under  
331 oedometric conditions, the homogeneous strain rate reads:

$$\underline{d} = -\frac{\dot{\delta}/h_0}{1-\delta/h_0} \underline{e}_v \otimes \underline{e}_v \quad (41)$$

332 For a prescribed deformation rate  $\underline{\underline{d}}$ , the problem consists in solving the set of equations  
 333 presented in sections 2.1 and 2.2 together with eq. (22) of section 2.4. The hardening law  
 334 indicates that  $p_c = 0$  when  $\varphi = \varphi_0$ . This means that for any displacement  $\delta > 0$ , the REV  
 335 undergoes elastoplastic deformation. Developing the plastic consistency condition  $\dot{f} = 0$ :

$$\dot{f} = \frac{\partial f}{\partial \underline{\underline{\sigma'}}} : \underline{\underline{\dot{\sigma'}}} + \frac{\partial f}{\partial p_c} \frac{\partial p_c}{\partial J_p} \dot{J}_p = 0 \quad (42)$$

336 The rate of the Jacobian of plastic transformation is given by:

$$\dot{J}_p = J_p \text{tr} \underline{\underline{d}}^p \quad (43)$$

337 Introducing eqs. (1), (7) and (43) in eq. (42) allows deriving the plastic multiplier  $\dot{\chi}$ :

$$\dot{\chi} = \frac{\frac{\partial f}{\partial \underline{\underline{\sigma'}}} : \underline{\underline{C}} : \underline{\underline{d}}}{\frac{\partial f}{\partial \underline{\underline{\sigma'}}} : \underline{\underline{C}} : \frac{\partial g}{\partial \underline{\underline{\sigma'}}} - \frac{\partial f}{\partial p_c} \frac{\partial p_c}{\partial J_p} J_p \text{tr} \frac{\partial g}{\partial \underline{\underline{\sigma'}}}} \quad (44)$$

338 Finally, substitution of eqs. (7) and (44) in eq. (43) leads to the following nonlinear  
 339 differential equation that governs the evolution of  $J_p$ :

$$\frac{\dot{J}_p}{J_p} = \frac{\frac{\partial f}{\partial \underline{\underline{\sigma'}}} : \underline{\underline{C}} : \underline{\underline{d}}}{\frac{\partial f}{\partial \underline{\underline{\sigma'}}} : \underline{\underline{C}} : \frac{\partial g}{\partial \underline{\underline{\sigma'}}} - \frac{\partial f}{\partial p_c} \frac{\partial p_c}{\partial J_p} J_p \text{tr} \frac{\partial g}{\partial \underline{\underline{\sigma'}}}} \text{tr} \frac{\partial g}{\partial \underline{\underline{\sigma'}}} \quad (45)$$

340 A closed-form solution to this differential equation has been formulated in Bruch et al.  
 341 (2016) for the case of an associated plastic flow rule with linear expressions for the yield  
 342 surface and hardening law. However, this cannot be achieved for the present constitutive  
 343 model and a numerical procedure is necessary for this purpose.

344 The strategy adopted herein to evaluate  $J_p$  is to discretize the problem in time and to  
 345 numerically integrate eq. (45), then solving the resulting nonlinear problem explicitly. Once  
 346 the plastic Jacobian is determined for time  $t$ , the constitutive and complementary variables  
 347 can be accordingly updated. The increasing displacement  $\delta$  is applied until porosity reaches  
 348 its minimum value. Given the fact that the model assumes  $J^p \approx J = \Omega_t / \Omega_0$ , the displacement  
 349 needed to reach residual porosity is given by the following equation:

$$\delta(\varphi = \varphi_r) \approx h_0 \left( 1 - \frac{1 - \varphi_0}{1 - \varphi_r} \right) \quad (46)$$

350 Finally, a calibration procedure has to be carried out for each lithology of the geological  
 351 model in order to find the parameters  $C$  and  $m$  of the hardening law (22) that best fit the  
 352 burial trend described by Schneider's law (17). This optimization process has been  
 353 implemented in the mechanical code as a preprocessing step by applying an automatic  
 354 procedure based on the least squares method by repeatedly solving eq. (45) for different sets  
 355 of parameters.

356 **4.2 Sandstone and shale models**

357 Sandstone and shale lithologies have been chosen to illustrate the constitutive model  
 358 behavior and the results of the calibration procedure based on the oedometric compression  
 359 test. The material parameters for the basin compaction law (17) are presented in Table 1.  
 360

361 **Table 1:** Basin compaction law parameters.

| Parameter       | Sandstone | Shale |
|-----------------|-----------|-------|
| $\varphi_r$ (%) | 1         | 4     |
| $\varphi_a$ (%) | 14        | 12    |
| $E_a$ (MPa)     | 17        | 4     |
| $\varphi_b$ (%) | 30        | 44    |
| $E_b$ (MPa)     | 43        | 16    |

362  
 363 Table 2 gives the elastic and plastic parameters of the 3D poromechanical constitutive law,  
 364 where  $E_0$  and  $\nu_0$  respectively denote the initial Young modulus and Poisson's ratio of the  
 365 material. The plastic parameters  $M$ ,  $N$  and  $p_t$  are taken constant. The  $M$  and  $N$  values  
 366 correspond to a friction angle of  $30^\circ$  and to a dilatancy angle of  $10^\circ$ , respectively. The initial  
 367 and residual porosities come from the basin compaction law, with  $\varphi_0 = \varphi_r + \varphi_a + \varphi_b$ . The  
 368 values of  $C$  and  $m$  to be used in the hardening law (22) are obtained from the automatic  
 369 calibration procedure based on the REV solution of section 4.1.  
 370

371 **Table 2:** Poromechanical law parameters.

| Parameter       | Sandstone | Shale |
|-----------------|-----------|-------|
| $E_0$ (MPa)     | 9000      | 4000  |
| $\nu_0$         | 0.32      | 0.26  |
| $M$             | 1.2       | 1.2   |
| $N$             | 0.37      | 0.37  |
| $p_t$ (MPa)     | 0.25      | 0.25  |
| $\varphi_0$ (%) | 45        | 60    |
| $\varphi_r$ (%) | 1         | 4     |
| $C$ (MPa)       | 28.77     | 11.12 |
| $m$             | 1.09      | 1.17  |

372  
 373 The relation between porosity and vertical effective stress resulting from the oedometric  
 374 test is presented in Fig. 4 for both lithologies. The porosity values obtained from the basin  
 375 compaction law (17) are given as reference for the same range of stress. The results confirm  
 376 the ability of the constitutive model to provide similar porosity trends as those of the standard  
 377 basin simulator when the sediment material is submitted to oedometric conditions.  
 378

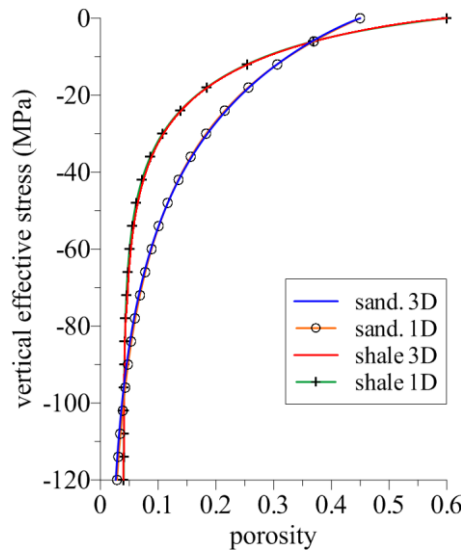


Fig. 4. Porosity versus vertical effective stress.

379  
380

381 According to eq. (46), the displacement  $\delta$  applied to the VER corresponds to 44.4% and  
 382 58.3% of deformation for the sandstone and shale materials, respectively. These deformation  
 383 levels emphasize the need to appropriately handle the problem of sedimentary basin  
 384 compaction in the framework of large irreversible strains.

## 385 5 Illustrative case

386 The iterative coupling scheme between 3D geomechanics and the standard basin code has  
 387 been used by petroleum exploration teams as a tool to better understand the geological history  
 388 of sedimentary basins in complex conditions. A recent work has been published by Berthelon  
 389 et al. (2021) demonstrating the importance of considering horizontal deformations to reliably  
 390 model the pore-pressure evolution of the Neuquén basin in Argentina.

391 In this work, a synthetic case has been chosen to illustrate the coupled procedure in a three-  
 392 dimensional framework. The main advantage of working with a simplified scenario is that it  
 393 makes it easier to investigate the constitutive model behavior and its impact on the evolution  
 394 of the sedimentary basin. The geological scenario concerns a large period of sediment  
 395 deposition and gravitational compaction followed by a tectonic phase leading to the  
 396 development of a characteristic buckle fold at the center of the model. The results obtained by  
 397 means of the coupled scheme are compared to those of the classical basin code before and  
 398 after tectonics.

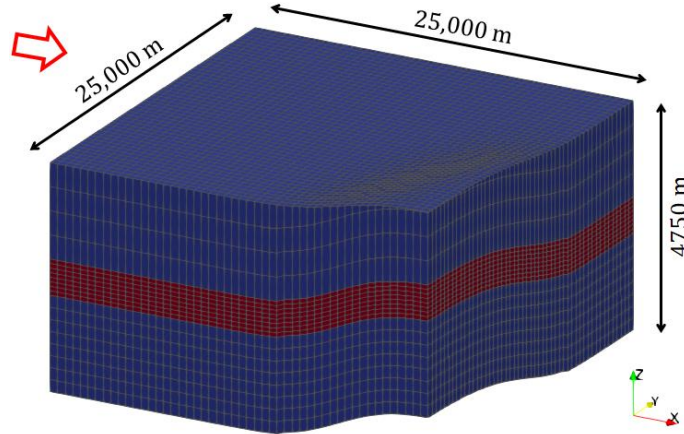
### 399 5.1 Problem statement

400 The deposition history of the sedimentary basin is given by the following geological  
 401 events: 1) a sandstone compartment is deposited in the first 20 My at constant rate of 144  
 402 m/My, 2) in the sequel, shale seal rocks are deposited during 30 My at 53 m/My, 3) finally, a  
 403 sandstone overburden is deposited in the last 40 My with an average rate of 58.5 m/My.  
 404 During these sequences, all stratigraphic units are disposed parallel to the horizontal plane.  
 405 Furthermore, both compartment and overburden are considered to be formed by the same  
 406 sandstone lithology.

407 Immediately after the deposition sequences, the basin is submitted to a lateral shortening of  
 408 4% during 4 My at constant rate. According to the geological scenario of the basin code  
 409 during this phase, a central region of the basin is progressively uplifted as a result of the  
 410 tectonics-induced deformation. As a consequence, a superficial thickness of the basin is  
 411 partially eroded.

412 The geometry is defined in the horizontal plane  $xy$  by a 50x50 km square. In the vertical  
 413 direction  $z$ , the basin is composed by 20 stratigraphic units: 8 layers for the compartment, 8  
 414 layers for the seal rocks and 4 layers for the overburden. The model is discretized by  
 415  $100 \times 100$  8-node hexahedral elements in the horizontal plane for a total of 200,000 elements.

416 The present day geometry of the basin is shown together with its lithology distribution in  
 417 Fig. 5, where the sandstone formations are drawn in blue and the shale rocks in red. Only a  
 418 quarter of the basin is presented due to the existence of two vertical planes of symmetry  
 419 intersecting each other at the center of the model. One can also observe the erosion process of  
 420 the superficial layer, starting at the limbs of the fold and reaching nearly 500 m of total  
 421 erosion at the hinge.  
 422



423 **Fig. 5.** Present day geometry and lithology distribution (vertical exaggeration: 3x). The red arrow indicates the  
 424 tectonic loading applied in the  $x$  direction.  
 425

426 In the mechanical code, the boundary conditions are applied as follows. During a non-  
 427 tectonic period, nodes of the bottom surface are fixed and the lateral sides of the model have  
 428 their normal direction restrained. During a tectonic sequence, the loading is simulated as an  
 429 imposed deformation rate. This is achieved by applying at each time step a linear  
 430 displacement field at the boundaries of the model corresponding to the desired kinematics.

431 In the basin code, the water table coincides with the top surface of the model during all the  
 432 simulation. The bottom and lateral surfaces are impermeable. For the sake of simplicity, the  
 433 thermal problem assumes an imposed temperature of  $T = 10^\circ\text{C}$  at the top surface of the  
 434 model combined with a prescribed vertical temperature gradient of  $T = 30^\circ\text{C}/\text{km}$ .

## 435 5.2 Material data

436 The sandstone and shale data correspond to those of section 4.2. In addition, the mass  
 437 density of the solid phase for the sandstone is  $\rho^s = 2675 \text{ kg}/\text{m}^3$ , and for the shale is  
 438  $\rho^s = 2645 \text{ kg}/\text{m}^3$ . Water is considered to be the only fluid saturating the porous material  
 439 with its mass density given by (Coussy, 2004):

$$440 \rho^f = \rho_0^f \exp\left(\frac{\Delta p}{K^f} - 3\alpha^f \Delta T\right) \quad (47)$$

440 where  $\rho_0^f = 1000 \text{ kg}/\text{m}^3$  is the reference fluid density,  $K^f = 2200 \text{ MPa}$  is the fluid bulk  
 441 modulus,  $\alpha^f = 7 \times 10^{-5} \text{ }^\circ\text{C}^{-1}$  is the fluid thermal dilation coefficient and  $T$  is the temperature.  
 442 The fluid viscosity is given by the following equation, with  $\eta^f$  in  $\text{MPa} \times \text{s}$  and  $T$  in degree

443 Celsius (Schneider, 1993):

$$\eta^f = \frac{1 \times 10^{-6}}{21.5 \left( T + \sqrt{8078 + T^2} \right) - 1200} \quad (48)$$

444 The permeability tensor reads (Schneider et al., 2000):

$$\underline{\underline{K}} = \underline{\underline{a}} k^f \quad (49)$$

445 where  $k^f$  is the intrinsic permeability coefficient and  $\underline{\underline{a}}$  is the anisotropy tensor defined as:

$$\underline{\underline{a}} = a_t (\underline{e}_{t1} \otimes \underline{e}_{t1} + \underline{e}_{t2} \otimes \underline{e}_{t2}) + a_n \underline{e}_n \otimes \underline{e}_n \quad (50)$$

446 with  $a_t$  and  $a_n$  respectively being the anisotropy coefficients related to the orthogonal  
447 tangential directions,  $\underline{e}_{t1}$  and  $\underline{e}_{t2}$ , and normal direction  $\underline{e}_n$  with respect to the layering plan of  
448 the rock in its local coordinate system.

449 The intrinsic permeability coefficient  $k^f$  of the porous medium is modeled through  
450 Kozeny-Carman formula:

$$k^f = \frac{0.2\varphi^3}{S^2(1-\varphi)^2} \text{ if } \varphi \geq 10\% \quad (51)$$

$$k^f = \frac{20\varphi^5}{S^2(1-\varphi)^2} \text{ if } \varphi < 10\% \quad (52)$$

451 where  $S$  is the specific surface area of the porous medium. The sandstone permeability tensor  
452 is taken isotropic with  $a_t = a_n = 1$  and  $S = 4 \times 10^5 \text{ m}^{-1}$ . For the shale material,  $a_t = 1$ ,  
453  $a_n = 0.02$  and  $S = 5 \times 10^7 \text{ m}^{-1}$ . These parameters have been chosen to make the sandstone  
454 material highly permeable during the whole simulation so that any overpressure development  
455 results from the low permeability shale layers. In addition, shale rocks permeability may be  
456 strongly anisotropic due to the presence of bedding, resulting in permeability values in the  
457 vertical direction magnitudes lower than in the horizontal direction (Pan et al., 2015). These  
458 microstructural effects are represented in the model by the adopted  $a_n$  coefficient.

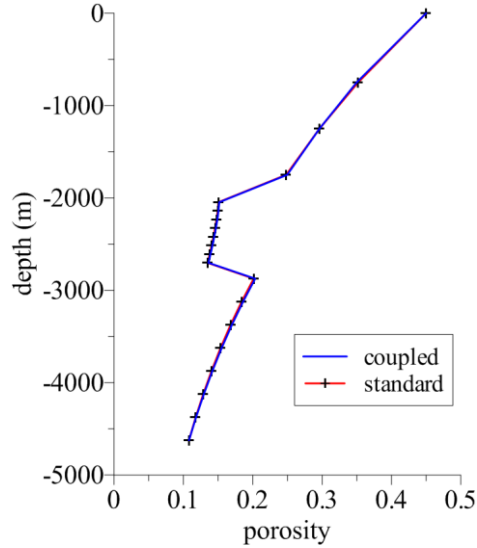
459 It should be emphasized that the Kozeny-Carman formula for porosity-permeability  
460 relation is mostly applicable to sediment particles with spherical structures. It is known that  
461 such approach fails to accurately predict the permeability of shale-like rocks for which an  
462 appropriate phenomenological or micromechanics-based model should be considered (Ma,  
463 2015; Revil and Cathles, 1999). However, such approach may be acceptable in the context of  
464 a synthetic sedimentary basin model.

### 465 5.3 Results: gravitational compaction

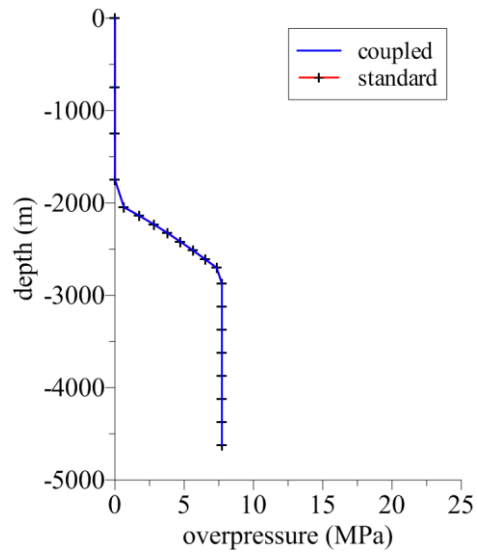
466 As burial proceeds and the basin deforms under oedometric conditions, all stratigraphic  
467 units remain parallel to each other. As a consequence, the resulting poromechanical fields at a  
468 given depth are constant with respect to the horizontal directions and a single profile is  
469 enough to illustrate their distribution in the basin. In the following part, the results of the  
470 gravitational compaction period are presented for the coupled as well as for the standard  
471 approaches.

472 The porosity, overpressure and effective stress profiles are presented in Figs. 6, 7 and 8,  
473 respectively. The top and the bottom of the seal rocks are located at  $z = -2047 \text{ m}$  and

474  $z = -2703 \text{ m}$ . It can be readily observed that both approaches provided the same results.  
475 This validates the requirement of the present constitutive model to represent the same  
476 behavior of the basin code under oedometric conditions, so that the iterative coupling scheme  
477 may affect the standard code simulation only when needed, i.e., when the horizontal  
478 deformations are not negligible.  
479



480 **Fig. 6.** Porosity profiles (gravitational compaction).  
481



482 **Fig. 7.** Overpressure profiles (gravitational compaction).  
483

484

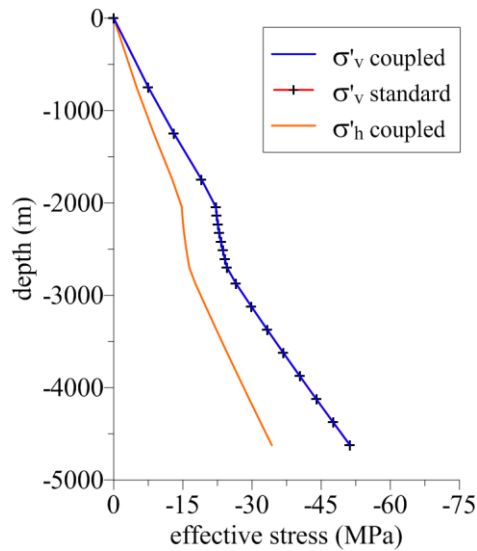


Fig. 8. Effective stress profiles (gravitational compaction).

485  
486

#### 487 5.4 Results: tectonic loading

488 The impact of tectonics on the present day state of the basin is analyzed in this section. It  
 489 concerns an imposed deformation of 4% in the  $x$  direction for a period of 4 My at constant  
 490 rate. The basin profiles given hereafter refer to the center of the model. The porosity,  
 491 overpressure and effective stress profiles are shown in Figs. 9, 10 and 11, respectively. The  
 492 top and the bottom of the seal rocks are located at  $z = -1076$  m and  $z = -1732$  m.

493 As expected, the results obtained from the coupled code are significantly different from  
 494 those provided by the classical basin code alone as the latter is not capable of taking  
 495 horizontal deformations into account. As a consequence, the basin code porosity distribution  
 496 is higher than the coupled one, except for the top compartment and bottom seal rocks which  
 497 resulted in similar porosity values. However, the mechanics of porosity loss in these zones  
 498 differs for each simulation. In the coupled case the porosity reduction results from tectonics,  
 499 whereas for the standard one it results from dissipation of the excess pore fluid pressure  
 500 cumulated during the sedimentation phase.

501 This can be verified by comparing Figs. 7 and 10, where the overpressure in the sandstone  
 502 compartment has reduced from 7.7 MPa to 1.3 MPa in the standard simulation. The opposite  
 503 has happened in the coupled calculation, where the tectonic loading has increased the  
 504 overpressure up to 23.3 MPa. As a consequence, the resulting vertical effective stress profiles  
 505 are particularly different between the two cases.

506  
507

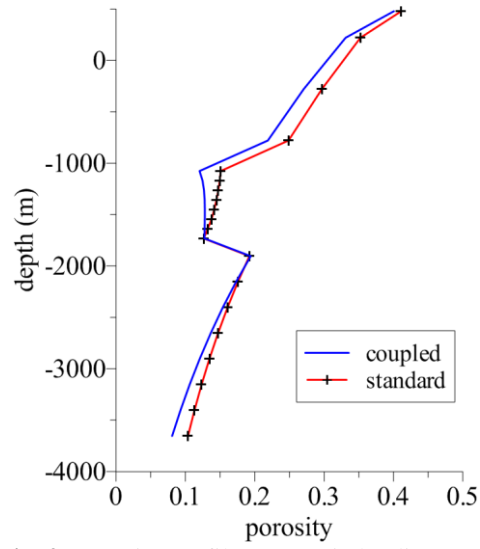


Fig. 9. Porosity profiles (tectonic loading).

508  
509

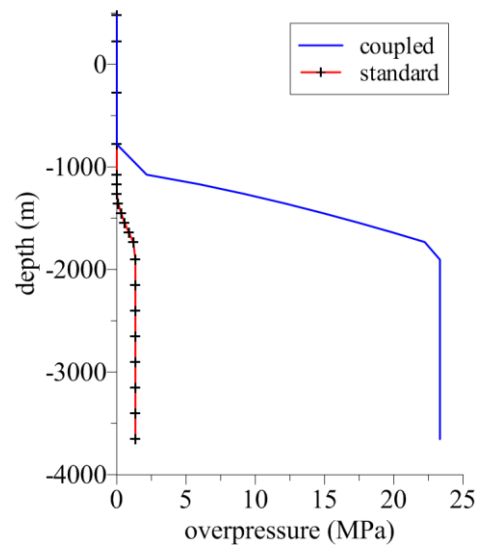
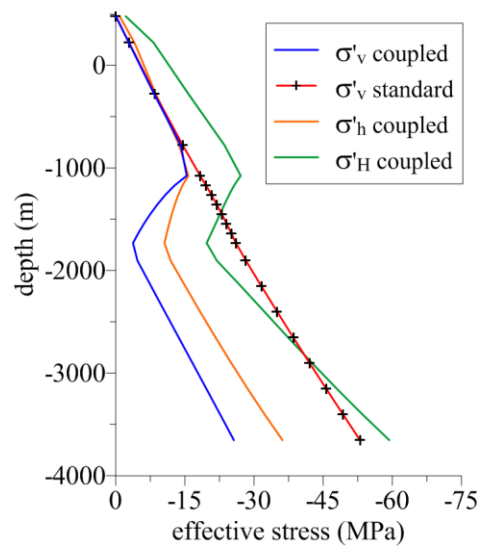


Fig. 10. Overpressure profiles (tectonic loading).

510

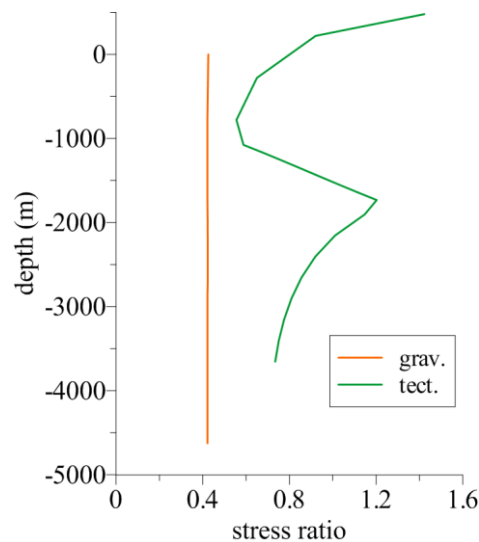


511  
512

Fig. 11. Effective stress profiles (tectonic loading).

513 The maximum compressive horizontal effective stress  $\sigma'_H$  and the minimum compressive  
 514 horizontal effective stress  $\sigma'_h$  cannot be compared between the two simulations since they  
 515 only exist in the coupled code. A three-dimensional geomechanics model is of interest for  
 516 industrial applications as it allows to identify critically stressed zones and to evaluate seal  
 517 rocks integrity. One way of doing this is to analyze the distribution of the stress ratio  
 518  $-q/(p'-p_t)$  to verify the proximity of the stress state to the  $M$  line of the yield surface (6). In  
 519 that matter, a change in the plastic regime from ductile failure (compaction) to brittle failure  
 520 (dilation) can be used as a preliminary criterion to predict the possibility of shear-induced  
 521 fractures in the basin (Bemer et al., 2004).

522 The stress ratio along the center of the model is shown in Fig. 12 for the coupled solution  
 523 before and after tectonics. It can be observed that during the burial phase a constant value of  
 524 0.42 is obtained for the whole basin. Nevertheless, the tectonic deformation has led the  
 525 bottom of the shale seal rocks and the sandstone formation at the hinge of the fold to present  
 526 stress ratio values higher than  $M = 1.2$ . Two different brittle behaviors are likely to occur for  
 527 the rocks in these two locations: for the lower shale rocks, the brittle behavior results from  
 528 pore-pressure build up in undrained conditions, whereas for the surface sandstones the brittle  
 529 behavior is related to a lack of confinement stress required to resist the shear efforts acting on  
 530 the top of the basin.  
 531



532 **Fig. 12.** Stress ratio  $-q/(p'-p_t)$  profiles before and after tectonics.  
 533

534 In what follows, the investigation of the constitutive model behavior will focus on the  
 535 evolution of the lower shale rock which presented a stress ratio higher than the  $M$  value in  
 536 Fig. 12 as the integrity of seal rocks is of major interest in sedimentary basin modeling. An  
 537 effective way to understand this failure mechanism is by drawing a stress path as shown in  
 538 Fig. 13 for the element in the base of the shale layer located at the center of the basin model.  
 539 The plastic yield surfaces before and after tectonics are also represented. From the moment  
 540 when the lower seal rock has been deposited until the end of the deposition period, the stress  
 541 path follows a straight line defining the porous material burial trend. As the lateral loading  
 542 starts, the deviatoric stress increases, while the mean effective stress decreases as a  
 543 consequence of the pore-pressure build up. The stress path follows the plastic yield surface  
 544 and slightly crosses the  $M$  line, leading to shear-induced dilation.  
 545

546  
547

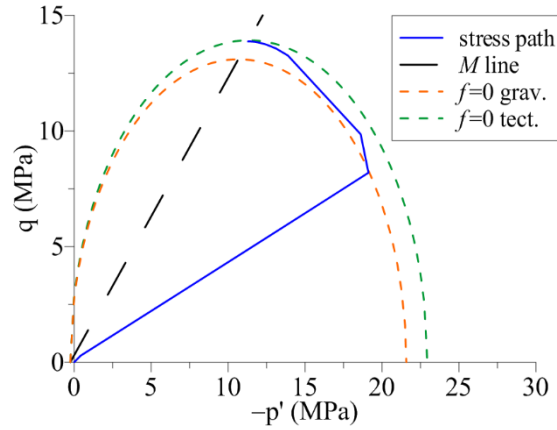


Fig. 13. Stress path of the lower seal rock.

548 To support the understanding of the basin physics and how it impacts the seal formation,  
549 the corresponding pore fluid, lithostatic and hydrostatic pressures are given in Fig. 14. It can  
550 be observed that during its first 50 My, the pore-pressure in the bottom shale rock is almost  
551 hydrostatic. The overpressure development accelerates after  $t = -24$  My during the last 20 My  
552 of the overburden deposition phase, when the shale rocks become sufficiently impermeable to  
553 behave as a compartment seal. At  $t = -4$  My the tectonic shortening starts and the pore-  
554 pressure significantly increases. At the same time, the erosion process takes place in the  
555 uplifted part of the basin, resulting in a constant decrease of the lithostatic and hydrostatic  
556 pressures. This phase is characterized by two opposite phenomena: the pore-pressure increase  
557 due to tectonics and its decrease associated to the lowering level of the water table. It is  
558 interesting to note that the maximum overpressure in the bottom shale rock occurs at  
559  $t = -2$  My, corresponding to 23.9 MPa.

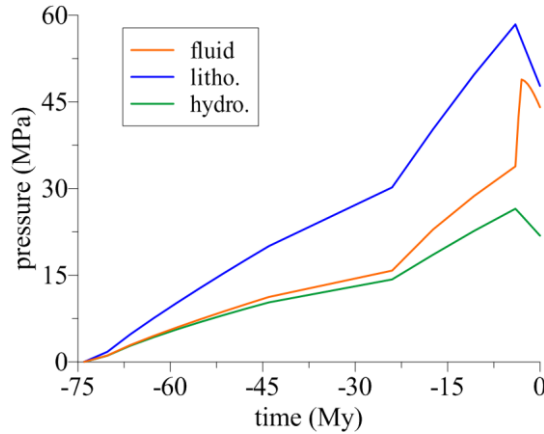


Fig. 14. Pore fluid, lithostatic and hydrostatic pressures evolution in the lower seal rock.

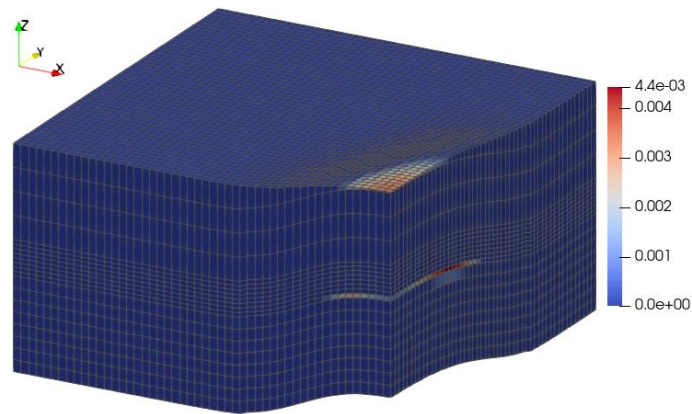
560  
561

562 The extension of brittle failure in the basin can be quantified by means of the equivalent  
563 von Mises strain  $\varepsilon_{eq}^p$  that occurs at the dilatant side of the Cam-Clay model:

$$\varepsilon_{eq}^p = \int_{t_1}^{t_2} \sqrt{\frac{2}{3} \underline{\underline{d}}^p : \underline{\underline{d}}^p} dt \quad (53)$$

564 where  $\underline{\underline{d}}^p$  corresponds to the deviatoric part of the plastic strain rate occurring between times  
565  $t_1$  and  $t_2$ . This quantity can be used as a first approach to visualize the potential distribution  
566 of natural fracturing in the basin as illustrated in Fig. 15, where  $\varepsilon_{eq}^p > 0$  indicates that the

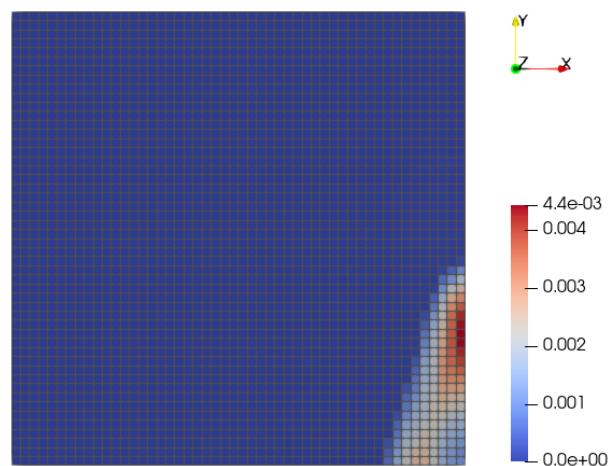
567 porous material has undergone shear-induced dilation. This is the case for a large region of  
 568 the bottom seal rocks and small regions of the top compartment and top overburden  
 569 sandstones.  
 570



571  
 572 **Fig. 15.** Present day equivalent shear strain of the basin (vertical exaggeration: 3x).

573 The present day equivalent shear strain of the bottom seal rocks is presented in Fig. 16.  
 574 The extent of the brittle failure region is 4.5 km in the  $x$  direction and 11.5 km in the  $y$   
 575 direction. It can be observed that the highest values occur at the limbs of the fold, with its  
 576 maximum located 7 km away from the center of the model. As discussed in Figs. 12, 13 and  
 577 14, the distribution of the brittle failure deformation in these rocks results from the multiple  
 578 phenomena occurring during the tectonic phase of the basin.

579 It is important to note that the consolidation pressure  $p_c$  remains the only hardening  
 580 parameter of the plastic model. The other parameters defining the size and shape of the yield  
 581 surface,  $p_t$  and  $M$ , are taken as constants, as well as parameter  $N$  defining the plastic flow  
 582 rule. This simplified approach is justified by the fact that the major concern at the present  
 583 moment corresponds to the ductile behavior (compaction) of the constitutive model.  
 584 Nevertheless, considering additional hardening laws such as the evolution of parameter  $p_t$   
 585 would affect the brittle behavior of the model, resulting in a different distribution of the  
 586 equivalent shear strain in Figs. 15 and 16. Such aspects remain to be addressed in a future  
 587 version of the model.  
 588



589  
 590 **Fig. 16.** Present day equivalent shear strain of the bottom seal rocks.

591

592 The same physics reported in this section have been obtained in the real case study of the  
593 Neuquén basin due to successive tectonic shortening phases related to the Andean subduction  
594 (Berthelon et al., 2021). A large zone of brittle failure has been observed in the low  
595 permeability Vaca Muerta formation resulting from the tectonic phase, with higher shear  
596 strain values at the edges of the western fold of the model.

597 In addition, similar material behavior has been observed by other authors such as Maghous  
598 et al. (2014) and Obradors-Prats et al. (2017). These authors worked on synthetic models to  
599 investigate the influence of lateral loadings in sedimentary basins by applying different rates  
600 of horizontal deformation under different states of basin consolidation.

601 It is important to note that this synthetic case has been developed to provide purely  
602 oedometric deformation during the whole deposition phase of the basin. For this reason, all  
603 stratigraphic units of the geological model are expressly deposited parallel to the horizontal  
604 plane. In real case basins this is not likely to occur and non-negligible horizontal deformations  
605 may occur even in the absence of tectonics.  
606

## 607 **6 Conclusions**

608 The paper presented a poromechanical constitutive law specifically devised to couple 3D  
609 geomechanics to classical sedimentary basin modeling. Based on the premise that the standard  
610 basin simulator provides consistent results for gravitational compaction, a new hardening law  
611 has been developed to make the mechanical code reproduce the same burial history of the  
612 basin code when submitted to oedometric conditions. Moreover, this turned out to be a good  
613 coupling strategy as it requires the mechanical solution to correct the basin code simulation  
614 only when horizontal deformations are not negligible, thus optimizing the iterative solution.

615 Referring to tectonics, the synthetic scenario of section 5 has revealed the lack of capacity  
616 of the standard basin code to deal with complex geological conditions. For such situations, the  
617 geomechanics coupling has proven its relevance to integrate horizontal deformations in the  
618 numerical simulation. The results of section 5.4 have shown that the lateral loading has led to  
619 significant overpressure build-up in the sandstone compartment, which in consequence  
620 resulted in a large surface of brittle failure in the shale seal rocks.

621 Although initially developed to serve hydrocarbon exploration teams, the proposed  
622 workflow may have an important role for the energy transition as the usage of the subsurface  
623 extends to other industrial applications such as CO<sub>2</sub> storage and geothermal energy. For such  
624 activities, a reliable basin simulation based on a comprehensive geomechanical framework  
625 may provide valuable information regarding critically stressed zones, seal rock integrity and  
626 fault stability. In addition, the resulting poromechanical fields can be used to define initial and  
627 boundary conditions of reservoir models.

628 Further developments are still ongoing to extend the geomechanics contribution in basin  
629 modeling. Regarding the constitutive model, the impact of brittle failure on rock permeability  
630 is an important issue to be addressed, as well as the incorporation of a chemo-mechanical  
631 coupling to account for fluid-rock interactions occurring at the microstructural level of the  
632 porous material. In what concerns the mechanical code, a new strategy of multi-domain  
633 parallel computation capable of dealing with large displacement contact problems is under  
634 development in order to simulate geological fault systems.  
635

## 636 **References**

- 637 Albertz, M., Sanz, P.F., 2012. Critical state finite element models of contractional fault-  
638 related folding: part 2. Mechanical analysis. *Tectonophysics*, 576–577, 150-170.  
639 Allen, P.A., Allen, J.R., 2005. *Basin analysis: principles and applications*. 2nd ed. Blackwell

640 Science Ltd.

641 Athy L.F., 1930. Density, porosity, and compaction of sedimentary rocks. *Am Assoc Pet Geol*

642 *Bull.* 14, 1-24.

643 Barnichon, J.D., Charlier, R., 1996. Finite element modelling of the competition between

644 shear bands in the early stages of thrusting: strain localization analysis and constitutive

645 law influence. *Geol Soc Spec Pub.* 99, 235-250.

646 Barthélémy, J.F., Dormieux, L., Maghous, S., 2003. Micromechanical approach to the

647 modelling of compaction at large strains. *Comput. Geotechnics* 30, 321–338.

648 Bathe, K.J., 1996. *Finite Element Procedures*. Prentice-Hall, Upper Saddle River.

649 Bemmer, E., Vincké, O., Longuemare, P., 2004. Geomechanical log deduced from porosity and

650 mineralogical content. *Oil Gas Sci. Technol. – Revue de l’IFP* 59, 405–426.

651 Bernaud, D., Deudé, V., Dormieux, L., Maghous, S., Schmitt, D.P., 2002. Evolution of elastic

652 properties in finite poroplasticity and finite element analysis. *Int. J. Numer. Anal.*

653 *Methods Geomechanics*, 26, 845–871.

654 Bernaud, D., Dormieux, L., Maghous, S., 2006. A constitutive and numerical model for

655 mechanical compaction in sedimentary basins. *Comput. Geotechnics* 33, 316–329.

656 Benjakul, R., Hollis, C., Robertson, H.A., Sonnenthal, E.L., Whitaker, F.F., 2020.

657 Understanding controls on hydrothermal dolomitisation: insights from 3D reactive

658 transport modelling of geothermal convection. *Solid Earth*, 11, 2439–2461.

659 Berthelon, J., Brüch, A., Colombo, D., Frey, J., Traby, R., Bouziat, A., Cacas-Stentz, M.C.,

660 Cornu, T., 2021. Impact of tectonic shortening on fluid overpressure in petroleum system

661 modelling: insights from the Neuquén basin, Argentina. *Marine and Petroleum Geology*

662 127.

663 Bjorlykke, K., 2010. *Petroleum Geoscience: from Sedimentary Environments to Rock*

664 *Physics*. Springer, Berlin.

665 Bjorlykke, K., 2014. Relationships between depositional environments, burial history and

666 rock properties. Some principal aspects of diagenetic process in sedimentary basins.

667 *Sediment. Geol.* 301, 1–14.

668 Borja, R.I., Lee, S.R., 1990. Cam-clay plasticity, part 1: implicit integration of elastoplastic

669 constitutive relations. *Comput. Methods Appl. Mech. Eng.* 78, 49–72.

670 Brüch, A., Guy, N., Maghous, S., 2019. Overpressure development in sedimentary basins

671 induced by chemo-mechanical compaction of sandstones. *Marine and Petroleum Geology*

672 104, 217–230.

673 Brüch, A., Maghous, S., Ribeiro, F.L.B., Dormieux, L., 2016. A constitutive model for

674 mechanical and chemo-mechanical compaction in sedimentary basins and finite element

675 analysis. *Int. J. Numer. Anal. Methods Geomech.* 40, 2238–2270.

676 Brüch, A., Maghous, S., Ribeiro, F.L.B., Dormieux, L., 2018. A thermo-poro-mechanical

677 constitutive and numerical model for deformation in sedimentary basins. *J. Pet. Sci. Eng.*

678 160, 313–326.

679 Buitter, S.J.H., Pfiffner, O.A., Beaumont, C., 2009. Inversion of extensional sedimentary

680 basins: a numerical evaluation of the localisation of shortening. *Earth Planet Sci Lett.*

681 288, 492-504.

682 Code\_Aster, EDF R&D, <http://www.code-aster.org>.

683 Coussy, O., 2004. *Poromechanics*. John Wiley & Sons Ltd, Chichester.

684 Crisfield, M.A., 1997. *Non-linear finite element analysis of solids and structures: essentials*.

685 John Wiley & Sons, Chichester.

686 Crook, A.J.L., Obradors-Prats, J., Somer, D., Peric, D., Lovely, P., Kacwicz, M., 2018.

687 Towards an integrated restoration/forward geomechanical modelling workflow for basin

688 evolution prediction. *Oil Gas Sci. Technol. – Rev. IFP Energies Nouvelles* 73, 18.

689 Crook, A.J.L., Willson, S.M., Yu J.G., Owen, D.R.J., 2006. Predictive modelling of structure

690 evolution in sandbox experiments. *J Struct Geol.* 28, 729-744.

691 Deudé, V., Dormieux, L., Maghous, S., Barthélémy, J.F., Bernaud, D., 2004. Compaction  
692 process in sedimentary basins: the role of stiffness increase and hardening induced by  
693 large plastic strains. *Int. J. Numer. Anal. Methods Geomechanics* 28, 1279–1303.

694 Dormieux, L., Maghous, S., 1999. Poroelasticity and poroplasticity at large strains. *Oil Gas*  
695 *Sci. Technol. – Revue de l’IFP* 54, 773–784.

696 Faille, I., Thibaut, M., Cacas, M.C., Havé, P., Willien, F., Wolf, S., Agelas, L., Pegaz-Fiornet,  
697 S., 2014. Modeling Fluid Flow in Faulted Basins. *Oil Gas Sci. Technol. – Rev. IFP*  
698 *Energies nouvelles* 69, 529–553.

699 Felippa, C.A., Park, K.C., Farhat, C., 2001. Partitioned analysis of coupled mechanical  
700 systems. *Comput. Methods Appl. Mech. Eng.* 190, 3247–3270.

701 Grigoli, F., Cesca, S., Priolo, E., Rinaldi, A.P., Clinton, J.F., Stabile, T.A., Dost, B.,  
702 Fernandez, M.G., Wiemer, S., Dahm, T., 2017. Current challenges in monitoring,  
703 discrimination, and management of induced seismicity related to underground industrial  
704 activities: a European perspective. *Rev. Geophys.*, 55, 310–340.

705 Guéguen, Y., Dormieux, L., Boutéca, M., 2004. Fundamentals of poromechanics. *Int. Geoph.*  
706 89, 1–54.

707 Gutierrez, M., Wangen, M., 2005. Modeling of compaction and overpressuring in  
708 sedimentary basins. *Mar. Petroleum Geol.* 22, 351–363.

709 Guy, N., Colombo, D., Frey, J., Cornu, T., Cacas-Stentz, M.C., 2019. Coupled modeling of  
710 sedimentary basin and geomechanics: a modified Drucker–Prager Cap model to describe  
711 rock compaction in tectonic context. *Rock Mech Rock Eng.* 52, 3627-3643.

712 Hamilton, E.L., 1959. Thickness and consolidation of deep-sea sediments. *Bull. Geol. Soc.*  
713 *Am.* 70, 1399–1424.

714 Hantschel, T., Kauerauf, A.I., 2009. Fundamentals of basin and petroleum systems modeling.  
715 Springer, Berlin.

716 Hashin, Z., 1983. Analysis of composite materials - a survey. *J. Appl. Mech.* 50, 481–505.

717 Hedberg, H.D., 1936. Gravitational compaction of clays and shales. *Am. J. Sci.* 31, 241–287.

718 Hubbert M.K., Rubey W.W., 1959. Role of fluid pressure in mechanics of overthrust faulting:  
719 I mechanics of fluid-filled porous solids and its application to overthrust faulting. *Bull*  
720 *Geol Soc Am.* 70, 115-166.

721 Jarosinski, M., Beekman, F., Matenco, L., Cloetingh, S., 2011. Mechanics of basin inversion:  
722 finite element modelling of the Pannonian Basin System. *Tectonophysics*, 502, 121-145.

723 Kim, J., Tchelep, H.A., Juanes, R., 2011. Stability and convergence of sequential methods for  
724 coupled flow and geomechanics: drained and undrained splits. *Comput. Methods Appl.*  
725 *Mech. Eng.* 200, 2094–2116.

726 Luo T., Qin Z., Feng X., Xia F., Yao Y., Sheng D., 2013. A symmetrisation method for non-  
727 associated unified hardening model. *Computers and Geotechnics* 52, 38–45.

728 Ma, J., 2015. Review of permeability evolution model for fractured porous media. *J. Rock*  
729 *Mech. Geotechnical Eng.* 7, 351–357.

730 Maghous, S., Brüch, A., Bernaud, D., Dormieux, L., Braun, A.L., 2014. Two-dimensional  
731 finite element analysis of gravitational and lateral-driven deformation in sedimentary  
732 basins. *Int. J. Numer. Anal. Methods Geomechanics*, 38, 725–746.

733 Mainguy, M., Longuemare, P., 2002. Coupling fluid flow and rock mechanics: formulations  
734 of the partial coupling between reservoir and geomechanical simulators. *Oil Gas Sci.*  
735 *Technol. – Revue de l’IFP* 57, 355–367.

736 Miranda, P.A.M.N., Vargas, E.A., Moraes, A., 2020. Evaluation of the modified Cam Clay  
737 model in basin and petroleum system modeling (BPSM) loading conditions. *Mar Pet*  
738 *Geol.* 112, 104-112.

739 Moscariello, A., 2019. Exploring for geo-energy resources in the Geneva Basin (Western

740 Switzerland): opportunities and challenges. *Swiss Bull. angew. Geol.* 24, 105-124.

741 Neto, E.A.S., Perić, D., Owen, D.R.J., 2008. *Computational methods for plasticity: Theory*

742 *and applications.* John Wiley & Sons, Chichester.

743 Nguyen, Q.S., 1977. On the elastic plastic initial boundary value problem and its numerical

744 integration. *Int. J. Numer. Meth. Eng.* 11, 817–832.

745 Nooraiepour, M., Mondol, N.H., Hellevang, H., Bjorlykke, K., 2017. Experimental

746 mechanical compaction of reconstituted shale and mudstone aggregates: Investigation of

747 petrophysical and acoustic properties of SW Barents Sea cap rock sequences. *Marine and*

748 *Petroleum Geology* 80, 265-292.

749 Obradors-Prats, J., Rouainia, M., Aplin, A.C., Crook, A.J.L., 2017. Assessing the implications

750 of tectonic compaction on pore pressure using a coupled geomechanical approach. *Mar.*

751 *Petroleum Geol.* 79, 31–43.

752 Obradors-Prats, J., Rouainia, M., Aplin, A.C., Crook, A.J.L., 2019. A diagenesis model for

753 geomechanical simulations: Formulation and implications for pore pressure and

754 development of geological structures. *Journal of Geophysical Research: Solid Earth*, 124.

755 Pan, Z., Ma, Y., Connell, L.D., Down, D.I., Camilleri, M., 2015. Measuring anisotropic

756 permeability using a cubic shale sample in a triaxial cell. *Journal of Natural Gas Science*

757 *and Engineering*, 26, 336-344.

758 Revil, A., Cathles III, L.M., 1999. Permeability of shaly sands. *Water Resour. Res.* 35, 651–

759 662.

760 Schmidt, V., McDonald, D.A., 1979. The role of secondary porosity in the course of

761 sandstone diagenesis. *Aspects Diagenesis* 26, 175–207.

762 Schneider, F., 1993. Modèle de compaction élasto-plastique en simulation de bassins. *Revue*

763 *de l'IFP* 48, 3-14.

764 Schneider, F., Potdevin, J.L., Wolf, S., Faille, I., 1996. Mechanical and chemical compaction

765 model for sedimentary basin simulators. *Tectonophysics* 263, 307–317.

766 Schneider, F., Wolf, S., Faille, I., Pot, D., 2000. A 3D Basin Model for Hydrocarbon Potential

767 Evaluation: Application to Congo Offshore. *Oil & Gas Science and Technology - Rev.*

768 *IFP* 55, 3–13.

769 Smith J.E., 1971. The dynamics of shale compaction and evolution of pore-fluid pressures. *J*

770 *Int Assoc Math Geol.* 3, 239-263.

771 Stricker, K., Grimmer, J.C., Egert, R., Bremer, J., Korzani, M.G., Schill, E., Kohl, T., 2020.

772 The Potential of Depleted Oil Reservoirs for High-Temperature Storage Systems.

773 *Energies*, 13, 6510.

774 Tada, R., Siever, R., 1989. Pressure solution during diagenesis. *Ann. Rev. Earth Planet. Sci.*

775 17, 89–118.

776 Tuncay, K., Ortoleva, P., 2004. Quantitative basin modeling: present state and future

777 developments towards predictability. *Geofluids* 4, 23–39.

778 Wood, D.M., 1990. *Soil Behaviour and Critical State Soil Mechanics.* Cambridge University

779 Press, Cambridge.

780 Zaoui, A., 2002. Continuum micromechanics: survey. *J. Engineering Mech.* 128, 808–816.

781 Zappone, A., Rinaldi, A.P., Grab, M., Wenning, Q.C., Roques, C., Madonna, C., Obermann,

782 A.C., Bernasconi, S.M., Brennwald, M.S., Kipfer, R., Soom, F., Cook, P., Guglielmi, Y.,

783 Nussbaum, C., Giardini, D., Mazzotti, M., Wiemer, S., 2021. Fault sealing and caprock

784 integrity for CO<sub>2</sub> storage: an in-situ injection experiment. *Solid Earth*, 12, 319–343.

785 Zienkiewicz, O.C., Taylor, R.L., 2000. *The Finite Element Method V.1: The Basis*, fifth ed.

786 Butterworth-Heinemann, Oxford.

787 Zivar, D., Kumar, S., Foroozesh, J., 2020. Underground hydrogen storage: a comprehensive

788 review. *International Journal of Hydrogen Energy*.